Energetic spin-polarized proton beams from two-stage coherent acceleration in laser-driven plasma

Zheng Gong [1,*], Yinren Shou,[1] Yuhui Tang [1], and Xueqing Yan[1,2,†]

[1]*SKLNPT, KLHEDP, CAPT, and School of Physics, Peking University, Beijing 100871, China*
[2]*CICEO, Shanxi University, Taiyuan, Shanxi 030006, China*

We propose a scheme to overcome the great challenge of polarization loss in spin-polarized ion acceleration. When a petawatt laser pulse penetrates through a compound plasma target consisting of a double layer slab and prepolarized hydrogen halide gas, a strong forward moving quasistatic longitudinal electric field is constructed by the self-generated laser-driven plasma. This field with a varying drift velocity efficiently boosts the prepolarized protons via a two-stage coherent acceleration process. Its merit is not only achieving a highly energetic beam but also eliminating the undesired polarization loss of the accelerated protons. We study the proton dynamics via Hamiltonian analyses, specifically deriving the threshold of triggering the two-stage coherent acceleration. To confirm the theoretical predictions, we perform three-dimensional PIC simulations, where unprecedented proton beams with energy approximating half GeV and polarization ratio $\sim 94\%$ are obtained.

I. INTRODUCTION

Spin is an essential intrinsic property of ions [1,2]. Energetic spin-polarized proton (SPP) beams are extensively used in fundamental physics [3,4] in exploring internal structures of nucleons [5,6], nonperturbative quantum chromodynamics [7–9], parity violating spin asymmetry in polarized proton colliders [10], and exotic phenomena within or beyond the standard model [11]. In nuclear physics, the SPP acts as a probe to measure the cross section of nucleus interaction [12–14], such as electron capture involved with the giant dipole resonance [15] and photon emission from nucleon bremsstrahlung [16]. Additionally, SPPs have also been pursued in industrial applications, e.g., electrochemical membrane optimization [17] and highly sensitive biomedical imaging [18]. Previously, energetic SPP beams were provided by traditional accelerators [19] equipped with the corkscrew-like magnets, i.e., *Siberian snakes* [20], to minimize proton polarization loss. The defect of such accelerators is too large in scale and budget. Therefore, an alternative compact and economical design for producing energetic SPP beams is highly desired.

Cutting-edge facilities based on the frontier optical technology [21,22] can realize pulse intensity far beyond 10^{20} W/cm^2 [23], which enables low-cost and efficient laser-plasma accelerators with a gradient over 100 GeV/m [24–26]. On the other side, owing to the ultraviolet photodissociation method [27–30], nuclear spin-polarized hydrogen densities extended to 10^{19} cm^{-3} with lifetimes near 10 ns have been achieved experimentally [31]. Encouraged by the above two breakthroughs, there is increasing interest in high efficiency laser-driven particle acceleration [32–34] and spin-polarized inertial confinement fusion [35] in prepolarized plasma.

However, up to now, only a few schemes have been proposed to accelerate polarized protons [36–38], and there is still a lack of an insightful understanding of the coupling effect between proton dynamics and collective plasma phenomena. As a result, the generated SPP beam is low quality, with energy $\sim$ 50 MeV and a polarization ratio $< 80\%$ [38], which inevitably limits the relevant applications requiring an energetic and highly polarized proton beam [4,13,16].

In this paper, we report an approach to generate highly energetic SPP beams whose maximum energy is close to 0.5 GeV and polarization ratio is as high as 94% by utilizing a petawatt laser. When the intense pulse propagates through a compound plasma target, a strong quasistatic longitudinal electric field (QSLEF) with a varying drift velocity repeatedly accelerates the polarized protons through a two-stage coherent process. Earlier, the protons are swiftly reflected by the forward moving QSLEF to arrive at a moderate velocity, while their spin polarization is largely preserved on account of the negligible net accumulation of spin modulation induced by the oscillating laser magnetic field. Later, as the drift QSLEF moves faster than these preaccelerated protons, the protons will be caught, trapped, and reflected again by the drift QSLEF to reach higher energy. Meanwhile, a vortex plasma magnetic field, issuing in the uncompensated transverse spin precession, merely leads to a minor polarization decrease of $\sim 6\%$ for the generated SPP beam. Because net spin precession occurs within a short duration in the second stage, the realized energetic SPP beam still maintains a high polarization ratio $\sim 94\%$, which would significantly facilitate the development of multiple branches of physics.

II. THEORY AND SIMULATION FOR ACCELERATION

The SPP dynamics is studied with the three-dimensional (3D) particle-in-cell (PIC) code EPOCH [39]. The $15 \times 20 \times 20\,\mu$m^3 simulation domain is discretized into $600 \times 400 \times 400$ grid cells. The compound target [see Fig. 1(a)] is a double

———————
[*]Present address: Max Planck Institute for Nuclear Physics, Saupfercheckweg 1, D-69117 Heidelberg, Germany.
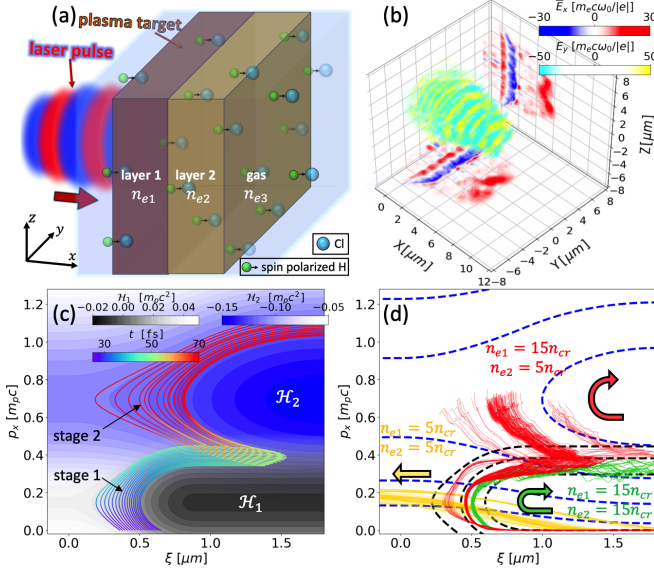[†]x.yan@pku.edu.cn

FIG. 1. (a) Schematic diagram of the compound plasma target irradiated by a laser pulse. (b) The volume rendering refers to the spatial distribution of field E_y, while the projection exhibits $\overline{E}_x$. (c) Theoretically predicted proton trajectories in (ξ, p_x) space, where the rainbow colors denote the time and the black (blue) color map displays the distribution of $\mathcal{H}_1$ ($\mathcal{H}_2$). (d) Typical proton trajectories extracted from 3D PIC simulations.

layer slab of near critical density carbon nanotube foams [40] mixed with prepolarized HCl gas [31]. The electron densities n_e of the first and second layers are $n_{e1} = 15n_{cr}$ and $n_{e2} = 5n_{cr}$, respectively. Here $n_{cr} \equiv m_e\omega_l^2/4\pi e^2$ is the classical critical density that determines plasma opacity in the nonrelativistic regime for a laser with frequency ω_l. m_e and e are the electron mass and charge. The first (second) layer target is placed at $0 \leqslant x < 3\,\mu\mathrm{m}$ ($3 \leqslant x \leqslant 6\,\mu\mathrm{m}$), where 40 particles per cell are chosen. The density profile of the hydrogen halides gas is a trapezoid with a flat top at $0 \leqslant x \leqslant 9\,\mu\mathrm{m}$ and a 1 $\mu\mathrm{m}$ ramp on both sides, where each cell is filled with 20 particles. The electron density of the prepolarized HCl is $n_{e3} = 0.8n_{cr}$, which is equivalent to an experimentally accessible hydrogen density of 4.9×10^{19} cm^{-3} [31]. A circularly polarized laser pulse of the Gaussian longitudinal envelope with intensity $a_0 \approx 70$, wavelength $\lambda = 1\,\mu\mathrm{m}$, spot size $5.8\,\mu\mathrm{m}$, and a duration of 30 fs in FWHM is focused at the plane $x = 0\,\mu\mathrm{m}$. Considering that such an ultraintense laser usually has a few hundred femtosecond prepulse with relativistic intensities before the main pulse, we perform additional one-dimensional PIC simulations to ensure that a prepulse with a duration of 400 fs and intensities up to $\sim 10^{18}$ W/cm^2 has an insignificant impact on the initial condition of the plasma target. Therefore, the scheme presented here for producing energetic SPP beams is valid and robust for the ultraintense pulse with a relatively high contrast ratio.

When the ultraintense pulse stably propagates inside the plasma, the drift QSLEF is sustained by the charge separation accumulated at the front edge of the laser pulse, as shown in Fig. 1(b), where the projection displays the distribution of the longitudinal electric field $\overline{E}_x$ averaged over two laser periods at section $z = 0$ and $y = 0$. The drift QSLEF $\overline{E}_x$, the

source of accelerated proton energies, moves along the laser propagation, as in previous results [41–45]. It is convenient to characterize the proton motion in the moving frame of the drift QSLEF in the one-dimensional circumstance. Here we adopt a local constant approximation, where the whole acceleration process is divided into several separate stages and in each of them the drift QSLEF is assumed to be independent of time. Thus, the properties of QSLEF are described by the drift velocity v_i, relative coordinate $\xi = x - v_i t$, field strength $E_i(\xi)$ ($\partial E_i/\partial t = 0$), and electric potential $\varphi_i(\xi)$ ($\partial\varphi_i/\partial t = 0$), where the subscript i denotes the ordinal number of stages. At each stage, after reformulating the proton dynamic equation in (ξ, p) space, a Hamiltonian is presented as $\mathcal{H}_i(\xi, p) = c\sqrt{m_p^2c^2 + p^2} - v_i p + |e|\varphi_i(\xi)$ [46,47], where c is the speed of light, m_p is the proton mass, and ξ_d (ξ_u) is the downstream (upstream) boundary of the electric potential. Given the conservation of the Hamiltonian $\mathcal{H}_i$ between points $(\xi_d, p_i^{r\pm})$ and (ξ_u, p_i) along the separatrix, where $p_i = m_p c\beta_i/\sqrt{1 - \beta_i^2}$ and $\beta_i = v_i/c$, the upper and lower limit momenta $p_i^{r\pm}$ of protons along the contour of $\mathcal{H}_i(\xi, p) = \mathcal{H}_i(\xi_u, p_i)$ at the ith stage can be derived as $p_i^{r\pm}/(m_p c) = (\beta_i \mathcal{A}_i \pm \sqrt{\mathcal{A}_i^2 + \beta_i^2 - 1})/(1 - \beta_i^2)$, where $\mathcal{A}_i = |e|\varphi_i(\xi_u)/(m_p c^2) + 1/\gamma_i$ and $\gamma_i = 1/\sqrt{1 - \beta_i^2}$.

In order to realize the separate multiple-stage proton acceleration, the connection between stages i and $i + 1$ requires that the preaccelerated protons by stage i can be caught, trapped, and reaccelerated by the later stage, $i + 1$. From a mathematical aspect, this is equivalent to the contours of $\mathcal{H}_{i+1}(\xi, p) = \mathcal{H}_{i+1}(\xi_u, p_{i+1})$ and $\mathcal{H}_i(\xi, p) = \mathcal{H}_i(\xi_u, p_i)$ intersecting with each other. Consequently, the condition for successfully coupling these two stages is expressed as

$$p_i^{r+} - p_{i+1}^{r-} > 0, \tag{1}$$

where the value of $p_i^{r\pm}$ can be determined once β_i and $\varphi_i(\xi_u)$ are given. The solution of Eq. (1) is analytically derived as $\beta_{i+1} < \beta^*$, where

$$\beta^* \equiv \frac{-\tilde{\varphi}_{i+1}\tilde{p} + \tilde{p}\tilde{\gamma} + \sqrt{\tilde{\varphi}_{i+1}[2\tilde{\gamma} - \tilde{\varphi}_{i+1}]}}{\tilde{\gamma}^2}. \tag{2}$$

Here $\tilde{\varphi}_{i+1} = |e|\varphi_{i+1}(\xi_u)/(m_p c^2)$, $\tilde{p} = p_i^{r+}/(m_p c)$, and $\tilde{\gamma} = \sqrt{1 + \tilde{p}^2}$ are utilized. A detailed illustration of Eq. (1) and the derivation for obtaining Eq. (2) are given in the Appendix. The rainbow lines in Fig. 1(c) exhibit the theoretical proton trajectories in (ξ, p) space under a two-stage coherent acceleration, where the black (blue) contour represents the distribution of Hamiltonian $\mathcal{H}_1$ ($\mathcal{H}_2$) at the first (second) stage. For $\mathcal{H}_1(\xi, p)$, given that the parameters $\beta_1 = 0.145$ and $\tilde{\varphi}_1 \approx \tilde{\varphi}_2 \approx 0.0462$ are calculated from the moving longitudinal electric field E_x based on the 3D PIC simulation, as shown in Fig. 2(a), one can find $\tilde{p} = 0.466$ and $\tilde{\gamma} = 1.103$. Substituting these values into Eq. (2), we arrive at $\beta^* \approx 0.664 > \beta_2 = 0.574$, which indicates the success of connecting these two separate acceleration stages.

The representative proton trajectories within time $20 < t < 70$ fs extracted from 3D PIC simulations are shown as red lines in Fig. 1(d), where the background black (blue) dashed lines denote the contour of $\mathcal{H}_1$ ($\mathcal{H}_2$), the same as that in Fig. 1(c). The protons (in red) are reaccelerated to a momentum $p_x \approx 0.7m_p c$ at $t = 70$ fs in the second
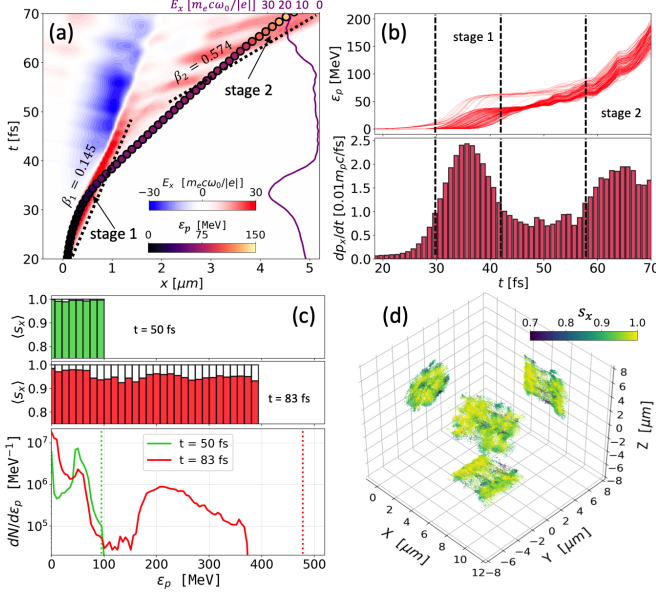
FIG. 2. (a) A proton trajectory (rendered with the magma colormap for its energy ε_p) inside the evolution of the on-axis accelerating field $E_x(y = 0, z = 0)$. (b) The time evolution of proton energy ε_p and momentum differential dp_x/dt. (c) The proton energy spectra (in the bottom panel) and the spin polarization ratio for different energy ranges (in the top panel), where the panels share the same horizontal axis. (d) The spatial distribution of the proton spin s_x at $t = 83$ fs.

Hamiltonian $\mathcal{H}_2(\xi, p)$ after being preaccelerated to $p_x \approx 0.3 m_p c$ in $\mathcal{H}_1(\xi, p)$. For comparison, green trajectories for the case of a uniform target with $n_{e1} = n_{e2} = 15 n_{cr}$ demonstrate that the protons merely experience the first stage of reflection in $\mathcal{H}_1(\xi, p)$. Additionally, the criterion of an initially resting proton being trapped in the Hamiltonian $\mathcal{H}_2(\xi, p)$ is calculated as $\beta^* \approx 0.300 < \beta_2 = 0.574$, and thus, the yellow trajectories representing the case of $n_{e1} = n_{e2} = 5 n_{cr}$ show that the protons quickly sliding away in $\mathcal{H}_2(\xi, p)$ are not trapped by the faster drift QSLEF.

To further understand the two-stage process, we visualize a typical proton trajectory in time resolved (x, t) coordinates [see Fig. 2(a)], where the background color denotes the strength of the electric field E_x $(y = 0, z = 0)$ at the central axis. When the laser bores a hole in the first layer slab, the proton is reflected by the laser pulse in the first stage to have a longitudinal velocity $\beta_x \approx 0.330 > \beta_1$. After the laser pulse penetrates through the first layer and irradiates the second layer slab, a faster drift QSLEF E_x with velocity $\beta_2 = 0.574 > \beta_x$ is generated to catch up with the protons and further accelerate them. The second stage of acceleration mainly occurs at $3 < x \lesssim 5\,\mu$m, which is in accordance with the location of the second layer slab. Another pronounced signal of the discontinuous two-stage acceleration is the purple line, which profiles the strength of accelerating field E_x imposed on the proton during $20 < t < 70$ fs. The top panel of Fig. 2(b) shows that the proton energies ε_p increase predominantly during $30 \lesssim t \lesssim 40$ fs and $60 \lesssim t \lesssim 70$ fs, and the maximum acceleration ratio $d\varepsilon_p/dt$ is up to 10 MeV/fs. The momentum differential dp_x/dt averaged over all typical

protons is illustrated in the bottom panel of Fig. 2(b), and the maximum accelerating gradient is over 60 TeV/m. One advantage of this mechanism is the energy enhancement induced by the second-stage acceleration, which is identified by the proton energy spectra at the end of two stages ($t = 50$ and 83 fs) in the bottom panel of Fig. 2(c), where the vertical dotted lines refer to the theoretically predicted maximum energies $\varepsilon_p^{\max} = [m_p^2 c^2 + (p^{r+})^2]^{1/2} = 94.7$ and 478 MeV in each stage. It is worth emphasizing that the key point in this mechanism is the double occurrence of spatial coherence between the SPPs and the drift QSLEF inside these two plasma slabs. This is far different from energetic SPP bunches driven by magnetic vortex acceleration [38], where the proton energy is predominantly obtained when the laser pulse exits the rear surface of gas targets.

III. PROTON SPIN DYNAMICS

For the purpose of unveiling the coupling between the spin and laser-plasma effect, by utilizing the Thomas-Bargmann-Michel-Telegdi (TMBT) equation [48,49], we can characterize the proton spin dynamics as $d\mathbf{s}/dt = \mathbf{\Omega} \times \mathbf{s}$, where

$$\mathbf{\Omega} = \frac{e}{m_p c}\left[\frac{a\gamma + 1}{\gamma}\mathbf{B} - \frac{a\gamma}{\gamma + 1}(\boldsymbol{\beta} \cdot \mathbf{B})\boldsymbol{\beta} - \frac{a\gamma + a + 1}{\gamma + 1}\boldsymbol{\beta} \times \mathbf{E} \right]. \tag{3}$$

Here $a \approx 1.7928$ is the anomalous magnetic moment for protons. The spatial distribution of the spin s_x of protons with energy $\varepsilon_p > 50$ MeV manifests the high polarization of the generated energetic SPP beam [see Fig. 2(d)]. The top panel of Fig. 2(c) presents the polarization ratio $\langle S_x \rangle$ averaged over all protons within each energy bin. At the end of the first stage $t = 50$ fs, the averaged spin polarization ratio is $\langle S_x \rangle \approx 0.994$, while at $t = 83$ fs the ratio $\langle S_x \rangle \approx 0.946$. The polarization loss $1 - \langle S_x \rangle \approx 0.054$ at $t = 83$ fs is higher than that at $t = 50$ fs. Detailed tracking of the proton spin is illustrated below to explain the reason.

As evident from the dependence of proton spin s_x on time t in Fig. 3(b), the spin deterioration is exclusively encountered at the second stage, $t > 50$ fs. Accordingly, a net increment of undesired s_y and s_z is pronounced at $t > 50$ fs [see Fig. 3(c)], whereas a nonignorable oscillation takes place at the first acceleration stage $t < 40$ fs. Considering it is instructive to examine how $d\mathbf{s}/dt$ is governed by electric and magnetic fields, the spin differentials ds_x/dt, ds_y/dt, and ds_z/dt are illustrated in Figs. 3(d)–3(f). In the nonrelativistic regime $\gamma \sim 1$ and $\beta \ll 1$, the cycle frequency of spin precession can be approximated as $\mathbf{\Omega}_{\mathrm{non}} = e(a + 1)\mathbf{B}/m_p c$. At the first stage, $s_x \approx 1$ and $s_{y,z} \ll 1$ indicate that the terms incorporated with $s_{y,z}$ are negligible in the relations $ds_y/dt = \Omega_z s_x - \Omega_x s_z$ and $ds_z/dt = \Omega_x s_y - \Omega_y s_x$. As a result, the accumulation of undesired spin predominantly originates from the transverse magnetic field as $ds_y/dt = e(a + 1)B_z s_x/m_p c$ and $ds_z/dt = -e(a + 1)B_y s_x/m_p c$. The dashed black lines in Figs. 3(d)–3(f) correspond to the results governed by $\mathbf{\Omega}_{\mathrm{non}}$ under nonrelativistic approximation, which are in reasonable agreement with the relativistic results. At the first stage, the oscillation of $ds_{y,z}/dt$ comes from the laser magnetic field imposed on the
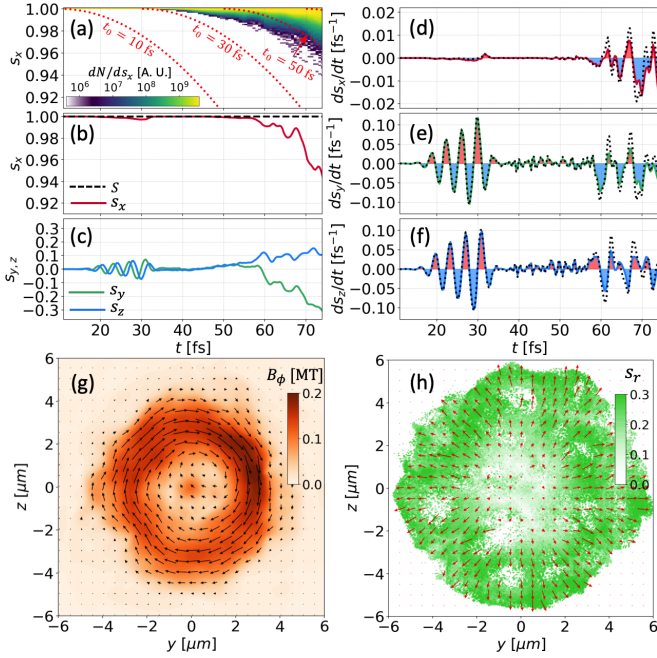
FIG. 3. (a) Time-resolved proton spin distribution, where the red lines illustrate the theoretical prediction of Eq. (4). (b)–(f) Time evolution of different variables, s_x, $s_{y,z}$, ds_x/dt, ds_y/dt, and ds_z/dt. (g) The distribution of field strength B_ϕ, where the arrows denote the field direction. (h) The distribution of spin $s_r = (s_y^2 + s_z^2)^{1/2}$; the arrows mark its direction.

FIG. 4. (a) Cutoff energies of generated SPP beams versus plasma electron density n_{e1} of the first layer target. (b) Averaged spin polarization ratio (gray triangles) and total charge (blue circles) of the generated SPP beam as a function of density n_{e1}.

proton. Nevertheless, because of the periodic symmetry of the laser field, the net accumulated $s_{y,z}$ is inappreciable, and thus, the initial favorable spin s_x characterized by $ds_x/dt = \Omega_y s_z - \Omega_z s_y$ is still largely preserved.

At the second stage, the oscillation symmetry in $ds_{y,z}/dt$ is broken [see Figs. 3(e)–3(f)], and a gradual increment occurs for $s_{y,z}$ [see Fig. 3(c)], which is accompanied by the decrease of s_x. The reason is that a strong vortex plasma magnetic field [50–52], sustained by the forward moving electron current when the laser pulse penetrates through the slab's second layer, contributes to a net accumulated precession for $s_{s,y}$. The distribution of magnetic field strength $B_\phi = (B_y^2 + B_z^2)^{1/2}$ at $t = 83$ fs averaged over $3 \leqslant x \leqslant 6\,\mu$m is exhibited in Fig. 3(g), where the field B_ϕ is along the azimuthal direction and its strength is as high as 0.2 MT. Following the above nonrelativistic assumption, we can rearrange the secondary differential of spin s_x as $d^2 s_x/dt^2 + \Omega_\phi^2 s_x \approx 0$ and subsequently obtain the solution as

$$s_x(t) \approx \cos\left[\frac{|e|(a+1)B_\phi}{m_p c}(t-t_0)\right], \qquad (4)$$

where $\Omega_\phi = e(a+1)B_\phi/m_p c$ and t_0 denotes the starting time of spin precession modulated by plasma vortex field B_ϕ. The theoretically predicted $s_x(t)$ of Eq. (4) is illustrated by red dashed lines in Fig. 3(a), where $B_\phi = 0.24$ MT is chosen and the prediction of $t_0 = 50$ fs is closest to the time-resolved spin distribution obtained from PIC simulations. This further confirms that the proton polarization loss is predominantly encountered at the second acceleration stage. The distribution of undesired transverse spin $s_r = (s_y^2 + s_z^2)^{1/2}$ of protons with
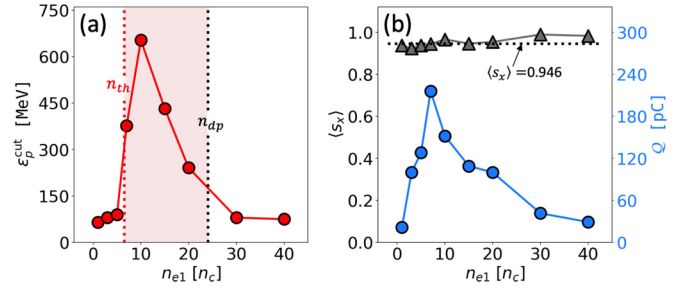
energy $\varepsilon_p > 50$ MeV [see Fig. 3(h)] demonstrates that the region with large s_r is coincident with the strong field B_ϕ and s_r is nearly neglectable near the central axis region $y = z = 0$. The red arrows in Fig. 3(h) mark the direction of transverse spin s_r, and its radial outward tendency is consistent with $ds_r/dt = \Omega_\phi \times s_x$ governed by the azimuthal plasma magnetic field B_ϕ.

IV. DISCUSSION AND SUMMARY

To confirm the feasibility and robustness of this scheme, we examine the dependence of the acceleration efficiency on the plasma density n_{e1} of the first layer target. A moderate density n_{e1} is prioritized to achieve the high energy of the generated SPP beams [see Fig 4(a)]. For relatively low density $n_{e1} < n_{th}$, the laser pulse readily penetrates through this transparent plasma target, where protons are not trapped but are swiftly surpassed by the drift QSLEF, similar to the scenario of $n_{e1} = n_{e2} = 5n_{cr}$ in Fig. 1(d). The threshold density can be estimated via $\beta_1(n_{th}) < \beta^*$, where $\beta_1(n_{th}) = \mathcal{K}_+ - \mathcal{K}_- - 1$ and $\mathcal{K}_\pm = [\frac{8a_0 n_c}{\pi^2 n_{th}}(\sqrt{1 + \frac{8a_0 n_c}{27\pi^2 n_{th}}} \pm 1)]^{1/3}$ are derived in relativistically transparent plasma [53]. Substituting $\varphi_1(\xi_u) = 0.065$ and $\tilde{p} = 0$ into Eq. (2), one finds $\beta^* \approx 0.355$, and the above density threshold can be determined as $n_{th} = 6.48n_{cr}$ [see Fig. 4(a)]. For relatively large density $n_{e1} > n_{dp}$, the laser pulse would be completely depleted and reflected by the accumulated overdense plasma edge before reaching the second layer due to its finite duration $\tau \sim 30$ fs. To estimate the density n_{dp}, we resort to the hole boring velocity $\beta_h = \sqrt{\Pi}/(1 + \sqrt{\Pi})$, where $\Pi = \frac{n_{cr}}{n_{e1}}\frac{Z_i m_e}{A_i m_i}\frac{1}{a_0^2}$ [43,54]. The criterion can be interpreted as $t_1 \beta_h c \sim L_1$, where $L_1 = 3\,\mu$m is the first layer thickness and t_1 is the interaction time. By utilizing the distance relation $\beta_h t_1 \approx t_1 - \tau$, the upper limit density is estimated as $n_{dp} \approx 24.02n_{cr}$. Within the range of $n_{th} < n_{e1} < n_{dp}$ [see Fig. 4(a)], the proton energy is dramatically enhanced compared with the other density conditions. In addition, the averaged spin polarization ratio [see Fig. 4(b)] manifesting this mechanism is favorable to preserving the proton spin polarization. $s_x = 0.946$ predicted by Eq. (4) indicates the insignificance of precession exerted on the protons spin by the vortex plasma magnetic field within a short time. The total charge of the generated SPP beams versus plasma density n_{e1} [see Fig. 4(b)] exhibits a variation tendency similar to that of the proton cutoff energies.
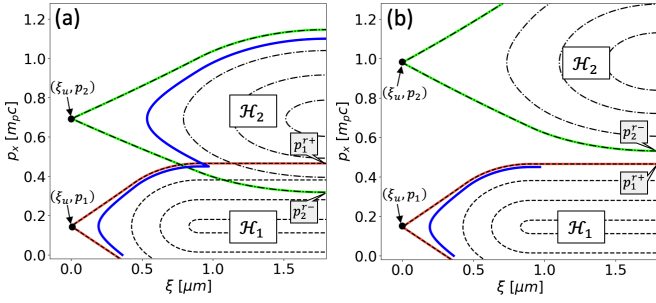
FIG. 5. The contours of the Hamiltonians $\mathcal{H}_1$ and $\mathcal{H}_2$ in (ξ, p) space, where the blue solid lines illustrate the evolution of a representative proton. (a) The case with $p_1^{r+} > p_2^{r-}$ and (b) the one with $p_1^{r+} < p_2^{r-}$. The lines highlighted in red and lime green correspond to the separatrices $\mathcal{H}_1(\xi, p) = \mathcal{H}_1(\xi_u, p_1)$ and $\mathcal{H}_2(\xi, p) = \mathcal{H}_2(\xi_u, p_2)$, respectively.

In conclusion, we identified and characterized a two-stage acceleration mechanism for generation of highly energetic SPP beams. In this scenario, the protons are accelerated by the drift QSLEF twice to achieve the energy enhancement. Meanwhile, the prepolarized protons substantially preserve their initial spin orientation because the polarization loss caused by spin precession exclusively occurs in the second acceleration stage within a relatively short time. Our mechanism based on laser-plasma acceleration, realizing a SPP beam with energy near 0.5 GeV and polarization over 90%, is an important step towards achieving the polarized ion beam quality required for the current frontiers of fundamental and nuclear physics.

APPENDIX

To explore the proton dynamics inside the two QSLEFs in (ξ, p) space, we adopt $\mathcal{H}_i$ and $\mathcal{H}_{i+1}$ to describe the Hamiltonian of a proton evolving within the slow and fast QSLEFs, respectively. In fact, the drift velocity β_{i+1} of the fast QSLEF should not be so large that the protons reflected by the slow QSLEF are able to catch up and gain more energy. From the aspect of the conserved Hamiltonian, to realize that the reflected protons from $\mathcal{H}_i$ can be trapped and efficiently accelerated by $\mathcal{H}_{i+1}$, the separatrices of $\mathcal{H}_i$ and $\mathcal{H}_{i+1}$ should intersect with each other, as shown in Fig. 5(a). For simplicity, i is set to 1 in Fig. 5, where the maximum (minimum) accessible momentum on the separatrix of $\mathcal{H}_1(\xi, p) = \mathcal{H}_1(\xi_u, p_1)$ $[\mathcal{H}_2(\xi, p) = \mathcal{H}_2(\xi_u, p_2)]$ can be calculated as p_1^{r+} (p_2^{r-}). It can be found from Fig. 5(a) that the occurrence of intersection between the two separatrices is equivalent to the condition of $p_1^{r+} > p_2^{r-}$. Therefore, the criterion for successfully coupling the proton dynamics inside these two Hamiltonian potentials can be expressed as

$$p_1^{r+} > p_2^{r-}, \tag{A1}$$

where

$$\begin{aligned} \frac{p_1^{r+}}{m_p c} &= \frac{\beta_1 \mathcal{A}_1 + \sqrt{\mathcal{A}_1^2 + \beta_1^2 - 1}}{1 - \beta_1^2}, \\ \frac{p_2^{r-}}{m_p c} &= \frac{\beta_2 \mathcal{A}_2 - \sqrt{\mathcal{A}_2^2 + \beta_2^2 - 1}}{1 - \beta_2^2} \end{aligned} \tag{A2}$$

can be found from a previous work [47]. Here the value of $\mathcal{A}_{1,2} = |e|\varphi_{1,2}(\xi_u)/(m_p c^2) + \sqrt{1 - \beta_{1,2}^2}$ can be determined once $\beta_{1,2}$ and $\varphi_{1,2}$ are given. By employing Eq. (A2), the criterion of Eq. (A1) can be rearranged as

$$\frac{\beta_1 \left[\frac{|e|\varphi_1(\xi_u)}{m_p c^2} + \sqrt{1 - \beta_1^2} \right] + \sqrt{\left[\frac{|e|\varphi_1(\xi_u)}{m_p c^2} \right]^2 + 2 \frac{|e|\varphi_1(\xi_u)}{m_p c^2} \sqrt{1 - \beta_1^2}}}{1 - \beta_1^2} > \frac{\beta_2 \left[\frac{|e|\varphi_2(\xi_u)}{m_p c^2} + \sqrt{1 - \beta_2^2} \right] - \sqrt{\left[\frac{|e|\varphi_2(\xi_u)}{m_p c^2} \right]^2 + 2 \frac{|e|\varphi_2(\xi_u)}{m_p c^2} \sqrt{1 - \beta_2^2}}}{1 - \beta_2^2}. \tag{A3}$$

Then the criterion can be analytically derived as

$$\beta_2 < \beta^* \equiv \frac{-\tilde{\varphi}_2 \tilde{p} + \tilde{p}\sqrt{1 + \tilde{p}^2} + \sqrt{\tilde{\varphi}_2 [2\sqrt{1 + \tilde{p}^2} - \tilde{\varphi}_2]}}{1 + \tilde{p}^2}, \tag{A4}$$

where $\tilde{p} = p_1^{r+}/(m_p c)$ and $\tilde{\varphi}_2 = |e|\varphi_2(\xi_u)/(m_p c^2)$ are adopted for convenience. It is worth pointing out that the threshold of Eq. (A4) will return to the more general form, i.e., Eq. (2), if the subscripts 1 and 2 are replaced by i and $i + 1$.

The validity of criterion (A1) can also be illustrated by the numerically resolved proton trajectories in (ξ, p) space, shown as the solid blue lines in Fig. 5. If $p_1^{r+} > p_2^{r-}$, the proton is captured by the faster QSLEF and evolves along a contour of $\mathcal{H}_2$, as shown in Fig. 5(a). In contrast, if $p_1^{r+} < p_2^{r-}$,

the proton does not experience an efficient acceleration at the second stage characterized by $\mathcal{H}_2$, as presented in Fig. 5(b). For the case exhibited in Fig. 5(a), after taking the chosen parameters $\beta_1 = 0.145$, $\beta_2 = 0.574$, and $\varphi_{1,2}(\xi_u) = 0.0462$ in Eq. (A4), one can find $\beta^* \approx 0.664 > \beta_2$, indicating the accomplishment of repeated proton reflection inside these two Hamiltonian potentials. By comparison, the parameters of the case in Fig. 5(b) are the same as those in Fig. 5(a) except for $\beta_2 = 0.7 > \beta^*$, which leads to the proton reflected in

$\mathcal{H}_1$ no longer being reflected in $\mathcal{H}_2$. After performing this examination, we claim that the analytically derived threshold of Eq. (A4) explicitly presents the condition of successfully coupling the two-stage acceleration. It should be noted that at the limit of $\tilde{p} \to 0$, the above threshold Eq. (A4) is equivalent to $\beta^* \equiv \sqrt{2\tilde{\varphi}_2 - \tilde{\varphi}_2^2}$, which is the upper limit velocity to achieve efficient acceleration for initially static protons [47].

The realization of the two-stage coherent acceleration is determined merely by the criterion described in Eq. (2). The importance is to find the appropriate decreasing density combination of the double layer slabs, i.e., n_{e1} and n_{e2}, to provide a proper drift velocity β_i and electric potential $\varphi_i(\xi_u)$ of the QSLEF. Some plasma kinetic effects, such as plasma instabilities [55], may deteriorate this matching relation between the laser intensity and plasma density. Therefore, a detailed investigation and systematic simulations are needed to figure out the exact dependence of the acceleration efficiency and obtained proton energy on laser intensity.

[1] D. J. Griffiths and D. F. Schroeter, *Introduction to Quantum Mechanics* (Cambridge University Press, Cambridge, 2018).

[2] S. Mane, Y. M. Shatunov, and K. Yokoya, Rep. Prog. Phys. **68**, 1997 (2005).

[3] M. S. Safronova, D. Budker, D. De Mille, D. F. J. Kimball, A. Derevianko, and C. W. Clark, Rev. Mod. Phys. **90**, 025008 (2018).

[4] E. C. Aschenauer, S. Fazio, J. H. Lee, H. Mäntysaari, B. S. Page, B. Schenke, T. Ullrich, R. Venugopalan, and P. Zurita, Rep. Prog. Phys. **82**, 024301 (2019).

[5] X. Ji, Phys. Rev. Lett. **78**, 610 (1997).

[6] D. de Florian, R. Sassot, M. Stratmann, and W. Vogelsang, Phys. Rev. Lett. **113**, 012001 (2014).

[7] L. Adamczyk, J. K. Adkins, G. Agakishiev, M. M. Aggarwal, Z. Ahammed, I. Alekseev, A. Aparin, D. Arkhipkin, E. C. Aschenauer, A. Attri *et al.* (STAR Collaboration), Phys. Rev. Lett. **116**, 132301 (2016).

[8] Y.-B. Yang, R. S. Sufian, A. Alexandru, T. Draper, M. J. Glatzmaier, K.-F. Liu, and Y. Zhao (χQCD Collaboration), Phys. Rev. Lett. **118**, 102001 (2017).

[9] C. Alexandrou, M. Constantinou, K. Hadjiyiannakou, K. Jansen, C. Kallidonis, G. Koutsou, A. V. Avilés-Casco, and C. Wiese, Phys. Rev. Lett. **119**, 142002 (2017).

[10] L. Adamczyk, J. K. Adkins, G. Agakishiev, M. M. Aggarwal, Z. Ahammed, I. Alekseev, J. Alford, C. D. Anson, A. Aparin, D. Arkhipkin *et al.* (STAR Collaboration), Phys. Rev. Lett. **113**, 072301 (2014).

[11] J. Jaeckel, M. Lamont, and C. Vallée, Nat. Phys. **16**, 393 (2020).

[12] L. Rosen, Science **157**, 1127 (1967).

[13] J. Tojo, I. Alekseev, M. Bai, B. Bassalleck, G. Bunce, A. Deshpande, J. Doskow, S. Eilerts, D. E. Fields, Y. Goto *et al.*, Phys. Rev. Lett. **89**, 052302 (2002).

[14] C. E. Allgower, K. W. Krueger, T. E. Kasprzyk, H. M. Spinka, D. G. Underwood, A. Yokosawa, G. Bunce, H. Huang, Y. Makdisi, T. Roser *et al.* (E925 Collaboration), Phys. Rev. D **65**, 092008 (2002).

[15] H. Glavish, S. Hanna, R. Avida, R. Boyd, C. Chang, and E. Diener, Phys. Rev. Lett. **28**, 766 (1972).

[16] P. Kitching, D. A. Hutcheon, K. Michaelian, R. Abegg, G. H. Coombes, W. K. Dawson, H. Fielding, G. Gaillard, P. Green, L. G. Greeniaus *et al.*, Phys. Rev. Lett. **57**, 2363 (1986).

[17] R. J. Kee, H. Zhu, B. W. Hildenbrand, E. Vøllestad, M. D. Sanders, and R. P. O'Hayre, J. Electrochem. Soc. **160**, F290 (2013).

[18] O. Zimmer, H. M. Jouve, and H. B. Stuhrmann, IUCrJ **3**, 326 (2016).

[19] M. Bai, T. Roser, L. Ahrens, I. G. Alekseev, J. Alessi, J. Beebe-Wang, M. Blaskiewicz, A. Bravar, J. M. Brennan, D. Bruno *et al.*, Phys. Rev. Lett. **96**, 174801 (2006).

[20] Ya. S. Derbenev and A. M. Kondratenko, Dokl. Akad. Nauk SSSR **223**, 830 (1975).

[21] D. Strickland and G. Mourou, Opt. Commun. **55**, 447 (1985).

[22] G. A. Mourou, T. Tajima, and S. V. Bulanov, Rev. Mod. Phys. **78**, 309 (2006).

[23] C. N. Danson, C. Haefner, J. Bromage, T. Butcher, J.-C. F. Chanteloup, E. A. Chowdhury, A. Galvanauskas, L. A. Gizzi, J. Hein, D. I. Hillier *et al.*, High Power Laser Sci. Eng. **7**, e54 (2019).

[24] T. Tajima and J. M. Dawson, Phys. Rev. Lett. **43**, 267 (1979).

[25] E. Esarey, C. B. Schroeder, and W. P. Leemans, Rev. Mod. Phys. **81**, 1229 (2009).

[26] A. Macchi, M. Borghesi, and M. Passoni, Rev. Mod. Phys. **85**, 751 (2013).

[27] T. Rakitzis, P. Samartzis, R. Toomes, T. Kitsopoulos, A. Brown, G. Balint-Kurti, O. Vasyutinskii, and J. Beswick, Science **300**, 1936 (2003).

[28] D. Sofikitis, L. Rubio-Lago, L. Bougas, A. J. Alexander, and T. P. Rakitzis, J. Chem. Phys. **129**, 144302 (2008).

[29] D. Sofikitis, P. Glodic, G. Koumarianou, H. Jiang, L. Bougas, P. C. Samartzis, A. Andreev, and T. P. Rakitzis, Phys. Rev. Lett. **118**, 233401 (2017).

[30] G. K. Boulogiannis, C. S. Kannis, G. E. Katsoprinakis, D. Sofikitis, and T. P. Rakitzis, J. Phys. Chem. A **123**, 8130 (2019).

[31] D. Sofikitis, C. S. Kannis, G. K. Boulogiannis, and T. P. Rakitzis, Phys. Rev. Lett. **121**, 083001 (2018).

[32] M. Wen, M. Tamburini, and C. H. Keitel, Phys. Rev. Lett. **122**, 214801 (2019).

[33] Y. Wu, L. Ji, X. Geng, Q. Yu, N. Wang, B. Feng, Z. Guo, W. Wang, C. Qin, X. Yan *et al.*, New J. Phys. **21**, 073052 (2019).

[34] Y. Wu, L. Ji, X. Geng, Q. Yu, N. Wang, B. Feng, Z. Guo, W. Wang, C. Qin, X. Yan *et al.*, Phys. Rev. E **100**, 043202 (2019).

[35] R. Hu, R. Zhou, Z. Tao, M. Lv, S. Zou, and Y. Ding, Phys. Rev. E **102**, 043215 (2020).

[36] A. Hützen, J. Thomas, J. Böker, R. Engels, R. Gebel, A. Lehrach, A. Pukhov, T. P. Rakitzis, D. Sofikitis, and M. Büscher, High Power Laser Sci. Eng. **7**, e16 (2019).

[37] M. Büscher, A. Hützen, I. Engin, J. Thomas, A. Pukhov, J. Böker, R. Gebel, A. Lehrach, R. Engels, T. P. Rakitzis *et al.*, Int. J. Mod. Phys. A **34**, 1942028 (2019).

[38] L. Jin, M. Wen, X. Zhang, A. Hützen, J. Thomas, M. Büscher, and B. Shen, Phys. Rev. E **102**, 011201(R) (2020).

[39] T. Arber, K. Bennett, C. Brady, A. Lawrence-Douglas, M. Ramsay, N. Sircombe, P. Gillies, R. Evans, H. Schmitz, A. Bell *et al.*, Plasma Phys. Controlled Fusion **57**, 113001 (2015).

[40] W. Ma, L. Song, R. Yang, T. Zhang, Y. Zhao, L. Sun, Y. Ren, D. Liu, L. Liu, J. Shen *et al.*, Nano Lett. **7**, 2307 (2007).

[41] X. Zhang, B. Shen, X. Li, Z. Jin, and F. Wang, Phys. Plasmas **14**, 073101 (2007).

[42] A. Robinson, M. Zepf, S. Kar, R. Evans, and C. Bellei, New J. Phys. **10**, 013021 (2008).

[43] A. Robinson, P. Gibbon, M. Zepf, S. Kar, R. Evans, and C. Bellei, Plasma Phys. Controlled Fusion **51**, 024004 (2009).

[44] N. Naumova, T. Schlegel, V. T. Tikhonchuk, C. Labaune, I. V. Sokolov, and G. Mourou, Phys. Rev. Lett. **102**, 025002 (2009).

[45] S. Weng, M. Murakami, P. Mulser, and Z. Sheng, New J. Phys. **14**, 063026 (2012).

[46] B. Shen, Y. Li, M. Y. Yu, and J. Cary, Phys. Rev. E **76**, 055402(R) (2007).

[47] Z. Gong, Y. Shou, Y. Tang, R. Hu, J. Yu, W. Ma, C. Lin, and X. Yan, Phys. Rev. E **102**, 013207 (2020).

[48] L. H. Thomas, London, Edinburgh, Dublin Philos. Mag. J. Sci. **3**, 1 (1927).

[49] V. Bargmann, L. Michel, and V. Telegdi, Phys. Rev. Lett. **2**, 435 (1959).

[50] A. Pukhov and J. Meyer-ter-Vehn, Phys. Rev. Lett. **76**, 3975 (1996).

[51] B. F. Lasinski, A. B. Langdon, S. P. Hatchett, M. H. Key, and M. Tabak, Phys. Plasmas **6**, 2041 (1999).

[52] T. Nakamura, S. V. Bulanov, T. Z. Esirkepov, and M. Kando, Phys. Rev. Lett. **105**, 135002 (2010).

[53] B. Liu, J. Meyer-ter Vehn, H. Ruhl, and M. Zepf, Plasma Phys. Controlled Fusion **62**, 085014 (2020).

[54] T. Schlegel, N. Naumova, V. Tikhonchuk, C. Labaune, I. Sokolov, and G. Mourou, Phys. Plasmas **16**, 083103 (2009).

[55] Y. Wan, I. A. Andriyash, W. Lu, W. B. Mori, and V. Malka, Phys. Rev. Lett. **125**, 104801 (2020).